Title:

Stress triggering in a rain-induced earthquake swarm in the Palghar region, western India

Authors:

Himangshu Paul[1,2] and M. Shekar[1]

Emails:

heman2007@gmail.com, m.shekar2k2@gmail.com

Affiliation:

[1]CSIR-National Geophysical Research Institute, Hyderabad-500007, India

[2]AcSIR-Academy of Scientific and Innovative Research, Ghaziabad, India

Corresponding author: Himangshu Paul

Preprint status:

This paper is a non-peer-reviewed preprint submitted to EarthArXiv

Journal submission status:

This paper has been submitted to ***Scientific Reports*** for peer review.

Stress triggering in a rain-induced earthquake swarm in the Palghar region, western India

Himangshu Paul[1,2] & M. Shekar[1]

[1]CSIR-National Geophysical Research Institute, Hyderabad, India.

[2]AcSIR-Academy of Scientific and Innovative Research, Ghaziabad, India

Corresponding author: Himangshu Paul*, heman2007s@gmail.com*

Abstract

Rain-triggered seismicity has been reported only in a few regions globally and is typically short-lived. However, an earthquake swarm, inferred to be rain-induced in previous studies, persisted with intense activity for over two years in Palghar, western India. Between January 2019 and November 2020, ~8,300 well-located earthquakes with horizontal and depth uncertainties ≤ 1.5 km were recorded at depths ≤ 10 km. Local magnitudes ranged from -0.1 to 4.6, with a magnitude of completeness of 1.4. Statistical analysis of the swarm revealed new insights into its underlying mechanisms. The swarm could be divided into phases based on the rise and fall of seismicity. Phases coinciding with the end of monsoon seasons showed high b-values, low seismic moment, and a gradual rise and fall of seismicity frequency, resembling cataclastic deformation. During other seasons, low b-values, high seismic moment, and a gradual rise followed by a rapid decline in seismicity frequency indicated stick-slip motion. Mainshock-aftershock sequences caused by stress triggering were found to co-exist within the swarm for most phases. The interplay of multiple causal mechanisms possibly sustained the swarm's longevity. This study is the first to report the presence of multiple causal mechanisms in a rain-induced swarm.

Keywords:

Fluid-induced swarm; Intra-plate earthquakes; b-value; Cataclasis; Omori's law; Monsoonal rain

Introduction

A swarm can be defined as a sequence of a large number of earthquakes without a prominent mainshock. Causal mechanisms of swarms are often associated with the movement of fluids. Therefore, swarms are commonly observed in volcanic regions where magma flow and associated pore pressure changes result in earthquakes [1-3]. In addition, direct or indirect involvement of fluids in processes such as industrial injection [4,5], CO_2 emission [6,7], reservoir loading [8], groundwater recharge [9], and rainfall [10,11] may also cause seismicity. However, the underlying processes governing earthquake swarms are often complex, involving other driving forces such as aseismic slip [12] or stress triggering [13]. Stress triggering refers to the phenomenon in which each event perturbs the local stress field, potentially initiating subsequent ruptures or critically loading nearby faults. This dynamic interaction may lead to a cascading sequence of events. In certain swarm sequences, multiple causal mechanisms have been seen to coexist [14-16]. In this context, we examine an intraplate earthquake swarm in the Palghar region of western India, where the underlying mechanisms remain poorly understood.

Palghar is located on the west coast of India within the Deccan Volcanic Province (Fig. 1 inset). Felt reports of seismicity in Palghar started in November 2018, with an M_L 3.2 earthquake recorded on November 11, 2018 [17]. The swarm sustained elevated seismic levels for more than two years, followed by a notable decline in frequency. Initially, the swarm was suggested to be caused by intraplate crustal stresses associated with late-Cretaceous mafic intrusions [18]. However, recent upper crustal velocity estimations for the region [19,20]

provide strong evidence for the presence of fluids. A few studies [17,21,22] argued the role of rainfall in seismogenesis, as they observed an increase in seismicity with rainfall intensity. Gahalaut et al. [22] showed that the pore pressure due to rainfall is significantly high at shallow depths (4-6 km) to promote seismicity. Sharma et al. [21] inferred the percolation of rainwater through a network of cracks and fissures as the cause of the seismicity. Peninsular India is devoid of volcanism since the Cretaceous, and the Palghar seismic zone is not proximal to any major surface reservoirs or known industrial extraction/injection activities. In the absence of the above factors, rainfall seems to be the only source of fluid.

However, rainfall-triggered swarms are generally short-lived, lasting a few hours to days only [10,11]. On the other hand, the Palghar swarm persisted for more than 2 years, marked by near-continuous seismic activity during the entire period (Fig. 2). This raises questions about the causal mechanism and prompts further inquiry into additional processes that may have sustained the prolonged seismicity. Swarms tend to be highly clustered in time and space, and the seismicity pattern is key for understanding the underlying processes [13]. Understanding the mechanism is important for predicting the swarm evolution as well as mitigating the hazard posed by it. Although previous studies indicate rainfall as the dominant cause of the swarm in Palghar, observation in terms of spatio-temporal variation is still lacking. In this study, we perform various statistical analyses to understand if there are other mechanisms, in addition to the fluid, that impart the swarm its continuity and longevity.

Results

Spatio-temporal distribution of earthquakes

About 8300 earthquakes recorded in the Palghar seismic network between January 2019 and November 2020 met our location error criteria and were used for further analysis. The

average horizontal (Δx) and depth (Δz) uncertainties of these earthquakes were found to be ~0.25 km and ~0.65 km, respectively. About 83% of the earthquakes were located within the 0-7 km depth range, with nearly all (98%) earthquakes confined within the top 10 km of the crust (Fig. 1). The earthquakes are seen to be distributed in two narrow N-S-oriented clusters. The second cluster emerged in November 2019 (Fig. 3a), nearly one year after seismic activity was first reported in Palghar, and is located ~5 km east of the initial cluster. Hereafter, we refer to these as the west and east clusters. The daily frequency of earthquakes seems to be highest at the end of the rainfall seasons (post-monsoons, Fig. 2). The time lag between peak monsoonal rainfall and seismicity is about 20-90 days, which is typical of fluid-induced seismicity [23]. However, we see that the earthquake frequency is high at other times also. Temporal variation of M_L reveals episodes wherein M_L gradually increases, reaches a maximum (usually exceeding 3.5), and then declines subsequently (Fig. 2c, d). These episodic cycles are repeated throughout the sequence, even in the absence of rainfall. A 30-day running average of the daily earthquake frequency also follows the same periodic rise and fall of seismicity (Fig. 2a, b). We refer to these episodes as distinct phases of the swarm. Different phases of swarms have also been seen elsewhere [24]. We name the phases as W1-W7 and E1-E4 for the west and east clusters, respectively. Typical monsoons in India start in June and may last until October. Phases W1, W2, W5, W6, E2, and E3 coincide with the post-monsoon seasons, while other phases commenced during the monsoon or pre-monsoon seasons.

Fig. 3a shows the temporal progression of seismicity in the map view, highlighting the non-stationary seismic activity within the two clusters. It also demonstrates that the key stages of the swarm development were triggered during the post-monsoon period (September to November) – (i) Seismic activity, possibly swarm initiation, was first reported during post-monsoon 2018 [17], (ii) the east cluster emerged during post-monsoon 2019, and (iii) new earthquakes appeared at the northern and southern extremities of the existing clusters during

post-monsoon 2020, possibly indicating an N-S expansion. At depth, earthquake hypocentres are remarkably confined in planar surfaces of ~2 km thickness (Fig. 3b). The west cluster aligns with a plane striking ~N8°E and dipping ~80° westwards, while the east cluster corresponds to a plane striking ~N5°W and dipping ~85° eastwards. However, earlier studies [17,21] suggested that both clusters were oriented eastward with a steep dip. All studies agree on the near-vertical nature of the seismicity planes, making it inherently difficult to distinguish between east- and west-dipping orientations. Moreover, slight variations in seismic velocity and network configuration can significantly affect focal depths [19] as well as the inferred orientation of seismicity planes. Furthermore, subsidiary faults may be present within these steep planes (See Discussion section). Therefore, irrespective of the orientation of the steep plane, our results remain consistent as focal depths reported in all studies are similar (within ~7 km).

Fig. 4 shows the variation of earthquake density (ρ_N – number of earthquakes per sq. km) within these steep planes during different swarm phases. In phase W1, a dense concentration of earthquakes ($\rho_N \gg 65$) is seen to be confined within a 3 km x 4 km area at shallow depths (1-5 km). Phase W2 possibly indicates continuation of seismicity in the same region. A similar high-density earthquake zone is observed during phase W5 ($\rho_N \approx 55$). In contrast, other phases exhibit dispersed seismicity ($\rho_N \leq 25$) distributed over a relatively broad region. Notably, phases W1 and W5 also display diffused seismicity in addition to concentrated clusters. In the east cluster, phase E2 shows moderate earthquake density ($\rho_N \approx 40$) but is distributed over a relatively wide region (10 km x 4 km) at shallow depths, while the remaining phases are characterised by dispersed seismicity. We do not observe any depth migration of seismicity, as the maximum depth reached during phase W1 is never exceeded (Fig. 4). We do observe some along-strike migration during November-December 2019 and September-November 2020, when seismicity migrated from the west cluster to the east cluster and towards

the southern end of the west cluster and the northern end of the east cluster, respectively (Fig. 3a).

Temporal variation of b-value and seismic moment

The local magnitude (M_L) of the earthquakes in Palghar varies between -0.1 and 4.6. The magnitude of completeness (M_c) has been estimated to be 1.4 [25]. The b-value from the frequency-magnitude relation [26] provides the relative proportion of small to large earthquakes, and can be an indicator of stress and associated processes [27,28]. Generally, $b > 1$ for swarm-type sequences, while $b \leq 1$ for typical mainshock-aftershock sequences [29]. The maximum likelihood b-value [30,31] of the entire Palghar sequence is found to be 0.89 ± 0.02, which seems small for a swarm. The b-value estimated for the entire sequence in earlier work is similar [32], although it is slightly higher when using a network closer to the seismic zone [21,33]. The temporal variation of b-value for each swarm phase is shown in Fig. 5a. For the west cluster, b-values are found to decrease systematically during phases W3, W4 and W7, while they increase abruptly during phases W5 and W6. Incidentally, phases W1-W2 and W5-W6 correspond to the post-monsoon seasons of 2018 and 2019, respectively. Similarly, W3-W4 and W7 are phases during the 2019 and 2020 monsoons, respectively. For the east cluster, phase E1 has a very small number of earthquakes and gives a b-value with a very large uncertainty. For the rest of the phases, b-values decrease slightly with time, with the highest value (~0.95) corresponding to phase E2 (post-monsoon). Although the b-values and their errors vary with different M_c values, the rise-and-fall pattern of the b-value across phases remains consistent (Fig. S1, Supplementary).

Earlier studies indicated a variable seismic moment (M_0) rate (daily average) for the Palghar sequence [19,22]. To gain a deeper insight, we investigated the temporal variation of M_0 for different clusters and phases. If M_0 does not vary significantly with time, the cumulative

seismic moment at any instance can be obtained by the product of the average seismic moment ($\bar{M}_0$) and the total number of earthquakes that have occurred upto that time. Mathematically, $\Sigma M_0 = i*\bar{M}_0$, where earthquake index i=1 for the 1st earthquake, i=2 for the 2nd earthquake, and so forth. This is particularly true for a swarm, where the magnitude range is limited and lacks an identifiable mainshock. Accordingly, ΣM_0 of earthquakes in the west cluster exhibits a linear relation (Fig. S2, Supplementary). However, for the east cluster, the ΣM_0 variation reaches as high as $i^{1.12}$. It implies that $\bar{M}_0$ increases by ~12% over time. When the exercise is repeated phase-wise, ΣM_0 for phases W3, W4, W7 is seen to follow a power law ($\propto i^{1.10}$), whereas phases W1, W5 and W6 exhibit a near-linear relation (Fig. 5b). Similarly, for the east cluster, E2 exhibits a power law ($\propto i^{1.15}$) while E3 and E4 follows a linear relation (Fig. 5c). In all sequences, the fit is consistently good across all earthquakes, except for the first 10-25 events. The initial earthquakes of any sequence are likely very small or deviate significantly from the mean value. Therefore, the trend requires about 25 earthquakes to stabilise.

The earthquake frequency and rate (for $M_L \geq M_c$) during different phases, such as W3, W4, and E2, show a gradual increase, followed by a sudden short-lived (1-2 days) peak and, ultimately, an abrupt decline over time (Fig. 5d, e). This pattern is characteristic of a stick-slip cycle [27,34]. However, the pattern is modified for phase W5, when we see a more symmetrical evolution with a gradual rise and fall in earthquake frequency (Fig. 5d).

Investigating mainshock-aftershock sequences

When the b-value decreases and the seismic moment increases episodically, stress triggering may play a role in seismogenesis [13,15]. The spatial distance between a mainshock and aftershocks generally indicates the extent of the slip or rupture propagation of the mainshock [35]. If earthquakes are generated by stress triggering, the subsequent earthquakes (aftershocks) should lie on the periphery or edge of the rupture area of the preceding earthquake

(mainshock). We test if this is true for the Palghar swarm. However, in a swarm, the earthquakes cannot be distinguished as mainshocks or aftershocks [36]. Therefore, we follow the methodology adopted by Hainzl and Fischer [13], where the largest earthquake within time windows of specified length (100 minutes, in our case) is assumed as the mainshock, and the earthquakes preceding and following it within the same window are assumed as foreshocks and aftershocks, respectively (See Methods for details). 220 mainshocks could be identified in the west cluster, while 86 mainshocks were found in the east cluster.

We see that the number of aftershocks in both the west and east cluster decays with time (Fig. 6a). The decay is represented by Omori's law [37], a distribution of the form $y = k/(t+c)$, where t is time, c and k are scalar constants. We found $k = 25$, $c = 0.8$ for the west cluster and $k = 8$, $c = 0.8$ for the east cluster. Similarly, the plot of aftershock density as a function of distance (Fig. 6b) shows a broad unimodal distribution characterised by (i) a gradual increase in density, and (ii) a systematic shift of the peak density towards greater distances with increasing mainshock magnitude. Generally, a larger magnitude earthquake produces a greater number of aftershocks and has a larger rupture area, which is reflected from the above result (Fig. 6b). The peak density represents the most probable distance of aftershocks from the mainshock for each magnitude group, which is confirmed by the increasing trend of the mean spatial separation or radius ($\bar{r}$) of aftershocks from the mainshock, with increase of magnitude (Fig. 6c). $\bar{r}$ for the west cluster increases as $k.10^{0.5M}$, consistent with the proposed relation, $\bar{r} \propto 10^{0.5M}$ [38]. Similarly, $\bar{r}$ for the east cluster initially follows a slightly higher scaling rate of $k.10^{0.55M}$ initially, but the rate of increase diminishes at higher magnitudes. The reduction is likely influenced by the gradual decline of seismic activity in the east cluster. For a dip-slip earthquake of M_w 1.8 ($\equiv M_L$ 1.8) and M_w 2.7 ($\equiv M_L$ 2.5), the rupture length is ~35 m and ~90 m, respectively [39]. The peak aftershock densities for M_L 1.5-2.2 and M_L 2.3-3.0 ranges appear at ~40 m and ~100 m, respectively (Fig. 6b), indicating that the aftershocks cluster just

beyond the rupture and therefore are triggered. All of the above results validate the presence of mainshock-aftershock sequences within the swarm.

Discussion

Earthquake activity in Palghar prior to 2018 is unknown, as none of the national and international agencies have reported any major or minor event in this region in the last 50 years. The swarm possibly initiated in November 2018, as seismicity was first reported during that period [17]. The region is free of magmatic fluid, major reservoirs, industrial injections, and other anthropogenic activities. As seen in this and previous studies, the seismicity frequency in the Palghar swarm is strongly influenced by rainfall, particularly when cumulative rainfall reaches its peak intensity by the end of the monsoon season. If the crust is sufficiently close to its critical state, even tiny pore pressure variations due to rainfall can trigger earthquakes [10]. It is likely that the initiation of the Palghar swarm followed a similar process. Unfortunately, we were not able to study the initiation of the swarm as the seismic network became operational in January 2019. However, we could record the later phases of the seismicity with high precision and observe their spatio-temporal variation. We discuss our observations in the context of existing knowledge.

Laboratory experiments have demonstrated that the frequency of seismic events varies with the magnitude of applied stress and the type of rock involved [27]. In brittle rocks, at low stress levels (<0.3 times the fracture strength), a small number of events arise from frictional sliding on existing cracks, but the activity dies out quickly. At stresses ≥ 0.6 times the fracture strength, seismic activity resumes due to brittle failure of asperities on the sliding surface and propagation of cracks [27,28,34]. Activity increases gradually as the stress approaches the fracture threshold. A sudden surge in seismicity is observed during fracture, followed by a sharp decline to a very low level. This rise and fall in event frequency represents a characteristic

cycle of stick-slip sliding [27,34]. At low stress levels, b-values are very high, whereas at high stress they tend to decrease [28]. In rocks that deform cataclastically, the number of events gradually increases with rising stress at a nearly constant rate until failure, after which activity declines gradually to a very low level [27]. Cataclasis involves stable intergranular frictional sliding and can cause brittle behaviour in porous rocks to transition to ductile behaviour under high pressure at constant temperature [40]. For such rocks, high b-values are observed across the entire stress range [28].

In this study, we observed high b-values during the post-monsoon phases, along with a decrease in average seismic moment (Fig. 5a-c). A high b-value implies a relatively large proportion of smaller earthquakes, which leads to a decrease in the average seismic moment. Earthquake frequency also exhibits a gradual rise and fall without any acceleration during this period (Fig. 5d), resembling the temporal pattern associated with cataclasis [27]. The Palghar region lies within the Deccan Volcanic Province, which hosts porous volcanic rocks formed during the Late Cretaceous. Seismicity in Palghar is confined to steeply dipping planar surfaces, which may represent pre-existing planes of weakness. However, focal mechanisms [22] show relatively gentle east- and west-dipping nodal planes with similar strikes, suggesting the presence of subsidiary faults dipping in either direction within these steep planes. Faults are characterised by low permeability and lower strength, promoting seismicity. Previous studies indicated that rainfall water likely percolated into the fault zone through networks of fractures [21]. Moreover, there is always a time lag before the induced fluid penetrates to a triggering depth [23]. During post-monsoon, when the cumulative rainfall reaches its peak or when the induced fluid penetrates sufficiently, it is plausible that large volumes of water become locally trapped within the fault zone. A significant hydraulic load can induce aseismic slip, potentially triggering seismicity in regions of asperities slightly away from the injection site [14,16,41]. The elevated pore pressure resulting from trapped water may have facilitated

cataclasis or aseismic deformation. Cataclastic pore-collapse due to hydrostatic loading has been observed for water-saturated basalts [42] and other rocks [43,44]. Evidence for aseismic deformation in the region comes from InSAR analysis, which revealed ~3 cm of fault zone subsidence between November 2018 and May 2019 [17]. The subsidiary faults within the steep plane likely accommodate the observed normal faulting [22], resulting in subsidence. The dense earthquake clustering observed in narrow zones within the shallow crust during post-monsoons (Fig. 4) may represent regions adjacent to zones of aseismic collapse.

During the pre-monsoon and monsoon seasons, the b-value is observed to be low, accompanied by an increase in average seismic moment (Fig. 5a-c), indicating a relatively higher proportion of larger earthquakes compared to smaller earthquakes. Larger earthquakes are seen to generate smaller earthquakes, which decay by Omori's law and are seen to cluster near the edge of the rupture area of the larger earthquakes (Fig. 6a, b). Moreover, the mean separation between the larger and smaller earthquakes increases with the magnitude of the larger events (Fig. 6c), and the peak aftershock concentration is consistent with the respective rupture length [39]. This behaviour is similar to mainshock-aftershock sequences in tectonic earthquakes. In stress triggering, stress redistributed by earthquakes generates subsequent events, which may act as secondary mainshocks and trigger further earthquakes, and so on. Stress triggering by successive earthquakes promotes rupture growth in a stick-slip fashion [13]. The prevalence of stick-slip cycles in both the west and east clusters (Fig. 5d, e) supports this inference. Unlike typical rainfall-triggered earthquakes, which tend to remain spatially confined [10,11], the seismicity spreading over a broad area within the confining plane and eventually reaching depths of ~10 km in Palghar can be explained by this mechanism, where the sequence of events results in an interconnected rupture area that expands with each event [13]. It seems stress triggering is active throughout the entire Palghar sequence as Omori's law is obeyed across all phases of the swarm, and widespread dispersed seismicity is observed in

nearly every phase (Fig. 4). Stress triggering, coupled with episodic aseismic collapse due to hydraulic load, may have contributed to the persistence of the Palghar swarm for over two years. Fluid-induced swarms exhibiting coseismic stress transfer have also been observed elsewhere [45]. However, such behaviour has not previously been reported in the context of rain-induced seismicity.

The east cluster emerged during the post-monsoon of 2019, raising the possibility that its formation was driven by high hydraulic load. However, a few earthquakes occurred during the preceding phase E1, between July and October. Although associated with large uncertainty, the b-value of these earthquakes are high (Fig. 5a) and show remarkable similarity to laboratory observations of brittle rocks under low-stress regimes [27]. Phase E2 exhibits stick-slip behaviour and a low b-value, indicative of brittle behaviour under mid-to-high stress levels or stress triggering. The spatial distribution reveals widespread, moderately dense seismicity, unlike the localised high-density seismicity observed during post-monsoons (Fig. 4). Therefore, it is likely that the east cluster was generated by failure due to stress propagation from the earthquakes in the west cluster, rather than by hydraulic loading. An earlier study [22] also supports this inference, where they indicated that Coulomb stress changes encouraged earthquake occurrence in the east cluster. The seismicity frequency and seismic moment in the later phases of the east cluster (E3, E4) indicate that activity is gradually declining. The interplay of periodic cataclasis and stress triggering in the west cluster appears to be absent in the east cluster, where most of the continuing seismicity likely results from stress triggering alone. This may imply that water did not percolate through the fault zone of the east cluster as efficiently as in the west cluster – an aspect that warrants investigation in future studies.

Conclusions

The statistical analysis of the Palghar swarm reveals a complex interplay of underlying processes. Despite near-continuous seismic activity spanning about two years, the swarm exhibited distinct temporal phases marked by the rise and fall of seismicity frequency and magnitude. Phases coinciding with monsoon season exhibited low b-value, high seismic moment and stick-slip frequency pattern. These features indicate possible pore-pressure increase and stick-slip fault motion due to rainwater percolating into the fault zone. In contrast, the post-monsoon phases showed relatively high b-values, low seismic moment, a gradual rise and fall in seismicity frequency, and dense localised clustering at shallow depths. These observations were found to be consistent with cataclasis or aseismic collapse under high hydraulic load from accumulated rainfall. Both mechanisms were primarily observed in the west cluster. In addition, the swarm exhibited signatures of stress triggering across all phases and both clusters as – (a) the density of smaller earthquakes decayed exponentially following Omori's law relative to the timing of the larger earthquakes, (b) smaller earthquakes were tended to concentrate near the periphery of the large earthquakes, (c) the separation between small and large events increased with the magnitude of the latter, and (d) the seismicity front advanced with each earthquake. The stress triggering process was persistent across all phases of both clusters, whereas fluid permeation and cataclasis acted as episodic, complementary processes during the monsoon and post-monsoon seasons. Their combined influence likely contributed to the longevity of the Palghar swarm. This study highlights the need for integrated models that consider both mechanical and hydrological drivers in swarms.

Methods

Earthquake location

Council of Scientific and Industrial Research - National Geophysical Research Institute (CSIR-NGRI), Hyderabad, set up a six-station broadband seismological network on January 30, 2019, to record the seismicity in the Palghar region (Fig. 1). More than 10000 earthquakes were recorded between January 2019 and November 2020 in this network. Initial phase picking was conducted manually and subsequently refined using waveform cross-correlation. This dataset was utilised by a previous study [19] to derive an optimal 1D velocity model of the region's upper crust, and rigorous synthetic tests were performed to assess its efficacy (Fig. S3, Supplementary). They used this model to relocate the earthquakes employing a probabilistic location program *NonLinLoc* [46], and a relative location program *HypoDD* [47]. The earthquake locations obtained in the above study were adopted for our analysis. For completeness, we briefly reiterate the methodology. *NonLinLoc* inversion was performed on an 80 km×80 km×40 km grid centred at 20.10°N, 072.90°E, with grid-node separation of 100 m. The grid-wise travel-time residual was efficiently searched using the Oct-tree Importance sampling algorithm. *NonLinLoc* converts pick errors and travel-time inaccuracies due to minute velocity variations into location error. By discarding events with large location errors, this approach yielded a robust set of well-constrained earthquakes. This methodology has been extensively used in various intraplate settings of India to obtain reliable earthquake locations [48,49]. A threshold location and depth error (Δx and Δz) of 1 km was chosen to obtain ~8300 well-located earthquakes.

To understand clustering of earthquakes, a relative location method, *HypoDD* [47], was employed to build a network of events in time and space. At first, the catalogue was analysed to find event pairs recorded at common stations. A network is created if an event is linked with

a prescribed number of events (N) within a search radius (*r*). In this study, *r* was initially taken to be 8 km while N was fixed to lie between 8 and 20. Larger N increases the computational cost exponentially. In the second stage, double difference travel-time residuals for all pairs were minimised iteratively using the singular value decomposition method. In 5 iterations, *r* was gradually reduced from 8 km to 1 km. The analysis primarily resulted in two clusters and a few sub-clusters within them (Fig. 3 and 4).

Magnitude and Seismic Moment estimation

The local magnitude (M_L) was computed using the relationship of Hutton & Boore [50], based on the maximum ground displacement amplitude corrected for local attenuation [51]. To estimate moment magnitude (M_W), a linear relation between M_L and M_W was calibrated using ~190 earthquakes spanning the entire M_L range. For each earthquake, the frequency spectrum obtained from a windowed (2-5 second) S-wave displacement was corrected for attenuation, geometrical spreading and site effects. Then the observed spectrum was best-fitted to the theoretical spectrum computed for a circular rupture, to estimate the corner frequency and low-frequency spectral flat. The seismic moment (M_0) was derived from the spectral flat using standard formulations [52]. These M_0 values for all stations of ~190 earthquakes were subsequently used to establish the linear relationship (Eqn. 1) between M_L and M_0 by least-squares regression (Fig. S4, Supplementary). This relation is used to estimate M_0 for any earthquake of magnitude M_L in the catalogue. M_0 is expressed in N-m.

$$M_0 = 10^{10.69+0.84M_L} \dots (1)$$

b-value estimation

The b-value is defined as the negative slope of the magnitude-frequency relation [26]. The b-value obtained by the least squares regression is often prone to various errors [53].

Moreover, least squares linear regression does not provide a unique trend, and multiple straight lines are required to fit the entire magnitude-frequency distribution of the Palghar sequence (Fig. S5, Supplementary). To compute a more robust b-value and its 95% confidence bound, we employed the maximum likelihood (MLE) method [30,31]. MLE assumes a truncated exponential distribution of magnitudes above a completeness threshold (M_c), providing a stable and unbiased estimate of b-value. The MLE b-value and its standard error are given by Aki [30] as

$$b = \frac{log_{10}e}{\langle M \rangle - \left(M_c - \frac{\Delta M}{2}\right)}; \sigma_b = \frac{b}{\sqrt{N}} \cdots (2)$$

where <M> is the average magnitude of events with magnitude $M \geq M_c$, ΔM is the catalogue bin width, and N is the total number of earthquakes with $M \geq M_c$. For robust estimation, M_c was determined using the maximum curvature method (MAXC) [54], as well as the Goodness-of-Fit (GoF) and Entire Magnitude Range (EMR) methods [25] The M_c obtained using MAXC was 1.15, whereas GoF and EMR yielded 1.4. Since b-values based on MAXC-derived M_c are often underestimated [25], we adopted $M_c = 1.4$. Nonetheless, b-values computed using different Mc were also examined to visualize the b-value variation pattern across phases (Fig. S1, Supplementary).

Mainshock-aftershock analysis

To identify mainshock and aftershocks and their spatio-temporal distribution, we employ the methodology of Hainzl & Fischer [13]. The largest earthquake within a time interval, say [T-δT, T+δT], is assumed as the mainshock, where T is the origin time of the mainshock. The time intervals which satisfy the following criteria were only chosen -- (i) the M_L of the mainshock is greater than a threshold value (M_T), and (ii) there exists a finite number of earthquakes with magnitude $\leq M_T$, apart from the mainshock, within that interval. The

earthquakes occurring within the interval [T-δT, T) are considered foreshocks, and those within the interval (T, T+δT] are considered aftershocks. For our study, δT = 100 minutes, M_T = 1.5, and the minimum number of aftershocks = 5. 220 mainshocks were identified in the west cluster and 86 in the east cluster. By combining data from all relevant time intervals, the number of aftershocks was computed as a function of their delay time relative to the mainshock. Similarly, the number of aftershocks occurring at a distance r ± δr relative to the mainshock is computed for different r. The aftershock density was obtained by normalising with the annular area 4πrδr. In our study, δr = 10 m and r was iterated from 20 m to 10 km. To enhance the trends, the aftershock densities corresponding to mainshocks within narrow magnitude bins were combined. The mean spatial extent of aftershock distribution ($\bar{r}$) for each mainshock magnitude is obtained by dividing the sum of all aftershock distances by the sum of the corresponding aftershock densities.

Figure Legends

Figure 1: Topographic map of the Palghar study area. ~8300 well-located earthquakes (with horizontal standard error ≤ 1.5 km and vertical standard error ≤ 1.5 km) recorded between January 2019 and November 2020 in the CSIR-NGRI network are plotted as circles, colour-coded by depth, over the regional topography. Seismic stations are shown as red triangles. The rain gauge station is shown as a green hexagon. The study region is marked by a square in the inset map of India (top left), which also outlines the extent of the Deccan Volcanic Province (DVP). The depth distributions of the earthquakes in the west and east clusters are shown as histograms of distinct colours (bottom right).

Figure 2: Temporal distribution of seismicity. (a), (b) Daily earthquake frequency (pink histogram), daily rainfall frequency (green), and annual cumulative rainfall (blue) are shown for the west and east clusters. Rainfall data is obtained from

https://giovanni.gsfc.nasa.gov/giovanni [55]. The nearest rain station is 15 km east of the seismic zone (Fig. 1). The 30-day running average of earthquake frequency is plotted as a thick black line. (c), (d) Temporal distribution of local magnitude (M_L) is shown for the west and east clusters. M_L sequences in both clusters are divided into distinct phases (W1-W7 & E1-E4), marked by dashed vertical lines based on the rise and fall of M_L values. See text for details. The red star in (c) denotes the timing of the first M_L 3.2 earthquake reported in Palghar [17].

Figure 3: Spatial distribution of seismicity. (a) Map view of the Palghar earthquake swarm, segregated by time. The earthquakes occurring every two months during 2019 and 2020 are represented by circles of different colours. A 3D view of the seismicity is shown from the southern horizon and an elevated southwest perspective. Seismicity in the west cluster (black dots) and east cluster (red dots) is sharply delineated along two distinct planes – AA' with a ~N8°E strike and 80° dip westward, and BB' with a ~N5°W strike and ~85° dip eastward, respectively. Around 200 earthquakes (blue open circles) do not lie in either plane.

Figure 4: Earthquake density (number per sq. km) for the west cluster projected onto plane AA' during phases W1-W7 and for the east cluster onto plane BB' during phases E1-E4. The corresponding colour scale is shown in one of the central panels.

Figure 5: Temporal variation of b-value, seismic moment and seismicity frequency. (a) Maximum likelihood b-values and their standard errors are plotted for different phases of the swarm in the west (black symbols) and east (green) clusters. (b), (c) Cumulative seismic moment (M_0) is plotted as a function of earthquake index (i) for each swarm phase in the west and east clusters, using different coloured symbols (diamonds). Theoretical trends proportional to i and $i^{1.10}$ in the west, and to i and i^{15} in the east cluster, are shown by solid and dashed lines, respectively. (d), (e) Daily earthquake frequency with $M_L \geq M_c$ is shown for phases W3-W5 and E1-E2 in the west and east clusters, respectively. Note that the trends require the initial 10-

25 events to stabilise. Phase boundaries are marked by vertical dashed lines. Coloured arrows indicate changes in frequency: Black ≡ gradual rise, blue ≡ gradual fall and red ≡ abrupt fall.

Figure 6: Plots showing aftershock characteristics. (a) Aftershock density as a function of delay time relative to the mainshock occurrence is shown for the west and east clusters using orange and sky-blue symbols, respectively. The mainshock is defined as the largest earthquake in a 100-minute window, while foreshocks and aftershocks precede and follow the mainshock in the same window. Theoretical trends following Omori's law are shown by magenta and blue dashed lines for the west and east clusters, respectively, with constants: k_1=25, k_2=8, and c=0.8. (b) Aftershock density as a function of distance (r) from the mainshock location is shown for the west (black) and east (red) clusters across different magnitude ranges. (c) Mean separation of the aftershocks ($\bar{r}$) from the mainshock is plotted as a function of magnitude (M). Theoretical trend lines based on a power-law and a linear trend are shown. Constants: k=0.06, a=1.55, and b=-2.30.

Acknowledgements

We thank the Director, CSIR-NGRI, for his kind permission to publish this work. We thank the project staff of the seismological observatory, CSIR-NGRI, for installing and maintaining stations in Palghar. We also acknowledge the two anonymous reviewers whose comments and suggestions have helped in improving the manuscript significantly. This work was carried out under CSIR-NGRI Project No. MLP-FBR-005 (MRK). The CSIR-NGRI reference number for this manuscript is NGRI/Lib/2022/Pub-008.

Author contributions

Himangshu Paul: Conceptualisation, Methodology, Statistical analysis, Software, Validation, Visualisation, Writing – original draft, Writing- review and editing; **M. Shekhar:** Investigation, Data curation, Project administration

Competing interests

The authors declare no competing interests.

Funding

The authors received No Funding for this work.

Data availability

All the statistical analyses were performed using the catalogue of well-located earthquakes, which is available from the corresponding author on reasonable request. Daily rainfall data from the beginning of 2018 to the end of 2020, used in this study, have been obtained from the NASA repository, https://giovanni.gsfc.nasa.gov/giovanni [55].

References

[1] Hill, D. P. et al. The 1989 earthquake swarm beneath Mammoth Mountain, California: An initial look at the 4 May through 30 September activity. *Bull. Seismol. Soc. Am.* 80(2), 325-339 (1990).

[2] Toda, S., Stein, R. S. & Sagiya, T. Evidence from the AD 2000 Izu islands earthquake swarm that stressing rate governs seismicity. *Nature* **419**, 58-61 (2002).

[3] Roman, D. C. & Cashman, K. V. The origin of volcano-tectonic earthquake swarms. *Geology* **34(6)**, 457-460 (2006).

[4] Shapiro, S. A. et al. Fluid induced seismicity guided by a continental fault: Injection experiment of 2004/2005 at the German Deep Drilling Site (KTB). *Geophys. Res. Lett.* **33(1),** L01309 (2006).

[5] Ellsworth, W. L. Injection-induced earthquakes. *Science* **341(6142)**, 1225942 (2013).

[6] Bräuer, K., Kämpf, H., Strauch, G. & Weise, S. M. Isotopic evidence (3He/4He, of fluid-triggered intraplate seismicity. *J. Geophys. Res.* **108**, 2070 (2003).

[7] Cappa, F., Rutqvist, J. & Yamamoto, K. Modeling crustal deformation and rupture processes related to upwelling of deep CO2-rich fluids during the 1965–1967 Matsushiro earthquake swarm in Japan. *J. Geophys. Res.* **114**, B10304 (2009).

[8] Hainzl, S., Aggarwal, S. K., Khan, P. K. & Rastogi, B. K. Monsoon-induced earthquake activity in Talala, Gujarat, India. *Geophys. J. Int.* **200(1)**, 627-637 (2014).

[9] Saar, M. O. & Manga, M. Seismicity induced by seasonal groundwater recharge at Mt. Hood, Oregon. *Earth Planet. Sci. Lett.* **214(3-4)**, 605-618 (2003).

[10] Hainzl, S., Kraft, T., Wassermann, J., Igel, H. & Schmedes, E. Evidence for rainfall-triggered earthquake activity. *Geophys. Res. Lett.* **33(19),** L19303 (2006).

[11] Husen, S., Bachmann, C. & Giardini, D. Locally triggered seismicity in the central Swiss Alps following the large rainfall event of August 2005. *Geophys. J. Int.* **171(3)**, 1126-1134 (2007).

[12] Vidale, J. E. & Shearer, P. M. A survey of 71 earthquake bursts across southern California: Exploring the role of pore fluid pressure fluctuations and aseismic slip as drivers. *J. Geophys. Res.* **111**, B05312 (2006).

[13] Hainzl, S. & Fischer, T. Indications for a successively triggered rupture growth underlying the 2000 earthquake swarm in Vogtland/NW Bohemia. *J. Geophys. Res.* **107(B12)**, 2338 (2002).

[14] Cornet, F. H., Helm, J., Poitrenaud, H. & Etchecopar, A. Seismic and aseismic slips induced by large-scale fluid injections. *Pure Appl. Geophys.* **150(3)**, 563-583 (1997).

[15] Hainzl, S. Seismicity patterns of earthquake swarms due to fluid intrusion and stress triggering. *Geophys. J. Int.* **159(3)**, 1090-1096 (2004).

[16] De Barros, L., Cappa, F., Deschamps, A. & Dublanchet, P. Imbricated aseismic slip and fluid diffusion drive a seismic swarm in the Corinth Gulf, Greece. *Geophys. Res. Lett.* **47(9)**, e2020GL087142 (2020).

[17] Sharma, V. et al. A long duration non-volcanic earthquake sequence in the stable continental region of India: The Palghar swarm. *Tectonophysics* **779**, 228-376 (2020).

[18] Srinagesh, D. et al. An appraisal of recent earthquake activity in Palghar region, Maharashtra, India. *Curr. Sci.* **118(10)**, 1592-1598 (2020).

[19] Paul, H., Sunilkumar, T. C., Gahalaut, V. K., Srinagesh, D. & Shekar, M. Significance of V_P/V_S ratio in locating earthquakes of a long-duration swarm in the western coast of India. *J. Seismol.* **28(3)**, 859-877 (2024).

[20] Kanaujia, J., Kumar, M. R., Vengala, P. K. & Shekar, M. Indication of Fluid-Driven Seismicity in the Palghar Region, India, from Local Earthquake Tomography. *Bull. Seismol. Soc. Am.* **115(2)**, 489-504 (2025).

[21] Sharma, V., Kumar, D., Sharma, B. & Chingtham, P. Characteristics of earthquake swarm activity observed in the Palghar region of Indian Peninsula from January 2019 to October 2020. *Quat. Sci. Adv.* **12**, 100099 (2023).

[22] Gahalaut, K. et al. Long duration non-volcanic and non-tectonic Palghar earthquake swarm in the stable continental region of India—Role of seasonal rainfall and earthquake cascading. *J. Seismol.* **26(3)**, 545-554 (2022).

[23] Talwani, P., Chen, L., & Gahalaut, K. Seismogenic permeability, k_s. *J. Geophys. Res.*, **112**, B07309 (2007).

[24] Fischer, T. The August–December 2000 earthquake swarm in NW Bohemia: the first results based on automatic processing of seismograms. *J. Geody.* **35(1-2)**, 59-81 (2003).

[25] Woesnner, J. & Wiemer, S. Assessing the quality of earthquake catalogues: Estimating the magnitude of completeness and its uncertainty, *Bull. Seismol. Soc. Am.*, **95(2)**, 684-698 (2005).

[26] Gutenberg, B. & Richter, C. Seismicity of the earth and associated phenomena. *Princeton Univ. Press* (1954).

[27] Scholz, C. H. Microfracturing and the inelastic deformation of rock in compression. *J. Geophys. Res.* **73(4)**, 1417-1432 (1968).

[28] Scholz, C. H. The frequency-magnitude relation of microfracturing in rock and its relation to earthquakes. *Bull. Seismol. Soc. Am.* **58(1)**, 399-415 (1968).

[29] Mogi, K. Some discussions on aftershocks, foreshocks and earthquake swarms-the fracture of a semi finite body caused by an inner stress origin and its relation to the earthquake phenomena. *Bull. Earthquake Res. Inst., Tokyo Univ.* **41**, 615-658 (1963).

[30] Aki, K. Maximum likelihood estimate of b in the formula log N= a - bM and its confidence limits. *Bull. Earthquake Res. Inst., Tokyo Univ*. **43**, 237-239 (1965).

[31] Utsu, T. A method for determining the value of b in a formula log N= a - bM showing the magnitude frequency relation for earthquakes. *Geophys. Bull. Hokkaido Univ*. **13**, 99-103 (1965).

[32] Mandal, P. et al. Characterization of earthquake hazard at the Palghar and Pulichintala swarm activity regions (India) through three-dimensional modelling of b-value and fractal (correlation) dimensions. *Nat. Hazards* **108**, 1183-1196 (2021).

[33] Nath, B., Singh, R. P., Gahalaut, V. K. & Singh, A.P. Dynamic Relationship Study between the Observed Seismicity and Spatiotemporal Pattern of Lineament Changes in Palghar, North Maharashtra (India). *Remote Sens.* **14**, 135 (2022).

[34] Byerlee, J. D. Frictional characteristics of granite under high confining pressure. *J. Geophys. Res.* **72(14)**, 3639-3648 (1967).

[35] Mendoza, C. & Hartzell, S. H. Aftershock patterns and main shock faulting. *Bull. Seismol. Soc. Am.* **78(4)**, 1438-1449 (1988).

[36] Mogi, K. The fracture of a semi-infinite body caused by an inner stress origin and its relation to the earthquake phenomenon (Second paper). *Bull. Earthquake Res. Inst. Univ. Tokyo* **41**, 595–614 (1963).

[37] Ōmori, F. On the after-shocks of earthquakes. *J. Coll. Sci. Imp. Univ. Tokyo* **7**, 111–200 (1894).

[38] Kanamori, H. & Anderson, D. L. Theoretical basis of some empirical relations in seismology, *Bull. Seismol. Soc. Am.*, **65(5)**, 1073– 1095, (1975).

[39] Leonard, M. Self-consistent earthquake fault-scaling relations. Bull. Seismol. Soc. Am. **104(6)**, 2953-2965 (2010).

[40] Wong, T. F. & Baud, P. The brittle-ductile transition in porous rock: A review. *J. Struct. Geol.* **44**, 25-53 (2012).

[41] Cappa, F., Scuderi, M. M., Collettini, C., Guglielmi, Y. & Avouac, J. P. Stabilization of fault slip by fluid injection in the laboratory and in situ. *Sci. Adv.* **5(3)**, eaau4065 (2019).

[42] Zhu, W., Baud, P., Vinciguerra, S. & Wong, T. F. Micromechanics of brittle faulting and cataclastic flow in Mount Etna basalt. *J. Geophys. Res.* **121(6)**, 4268-4289 (2016).

[43] Menéndez, B., Zhu, W. & Wong, T. F. Micromechanics of brittle faulting and cataclastic flow in Berea sandstone. *J. Struct. Geol* **18(1)**, 1-16 (1996).

[44] Zhu, W., Baud, P. & Wong, T. F. Micromechanics of cataclastic pore collapse in limestone. *J. Geophys. Res.* **115**, , B04405 (2010).

[45] De Barros, L. et al. Fluid-induced swarms and coseismic stress transfer: A dual process highlighted in the aftershock sequence of the 7 April 2014 earthquake (Ml 4.8, Ubaye, France). *J. Geophys. Res.* **124(4)**, 3918-3932 (2019).

[46] Lomax, A., Virieux, J. Volant, P. & Berge-Thierry, C. Probabilistic earthquake location in 3D and layered models: Introduction of a Metropolis-Gibbs method and comparison with linear locations. in *Advances In Seismic Event Location* (pp. 101-134). Dordrecht: Springer Netherlands (2000).

[47] Waldhauser, F. & Ellsworth, W. L. A double-difference earthquake location algorithm: Method and application to the northern Hayward fault, California. *Bull. Seismol. Soc. Am.* **90(6)**, 1353-1368 (2000).

[48] Paul, H., Ravi Kumar, M. & Kumar, S. Evidence for reactivation of new faults and seismicity migration away from the causative fault of the 2001 MW 7.7 Bhuj earthquake, western India. *Geophys. J. Int.* **226(3)**, 1800-1813 (2021).

[49] Gahalaut, K., Paul, H., Sunilkumar, T. C., Kumar, M. R., & Gahalaut, V. K. Earthquakes induced by rapid loading of faults during Pulichintala reservoir impoundment in the stable continental region of India. *Earth Space Sci.* **10(10)**, e2023EA002902 (2023).

[50] Hutton, L. K. & Boore, D. M. The ML scale in southern California. *Bull. Seismol. Soc. Am.* **77(6),** 2074-2094 (1987).

[51] Subhadra, N, & Shekar, M. The attenuation mechanism of high-frequency seismic waves in the Palghar swarm earthquake source area in Western India, *J. Asian Earth Sci.*, 276, 106306 (2024).

[52] Havskov, J. & Ottemöller, L. *Routine Data Processing in Earthquake Seismology: With Sample Data, Exercises and Software*. Springer, Berlin/Dordrecht/New York (2010).

[53] Utsu, T. Some problems of the frequency distribution of earthquakes in respect to magnitude (I). *Geophys. Bull. Hokkaido Univ.* **17**, 85-112 (1967).

[54] Wiemer, S. & Wyss, M. Minimum magnitude of completeness in earthquake catalogs: Examples from Alaska, the western United States, and Japan. *Bull. Seismol. Soc. Am.* **90(4)**, 859-869 (2000).

[55] Huffman, G., Stocker, E., Bolvin, D., Nelkin, E. & Tan, J. GPM IMERG Final Precipitation L3 1 day 0.1 degree× 0.1 degree v06, Edited by Andrey Savtchenko. *Goddard Earth Sciences Data and Information Services Center (GES DISC), Greenbelt, MD* (2019).

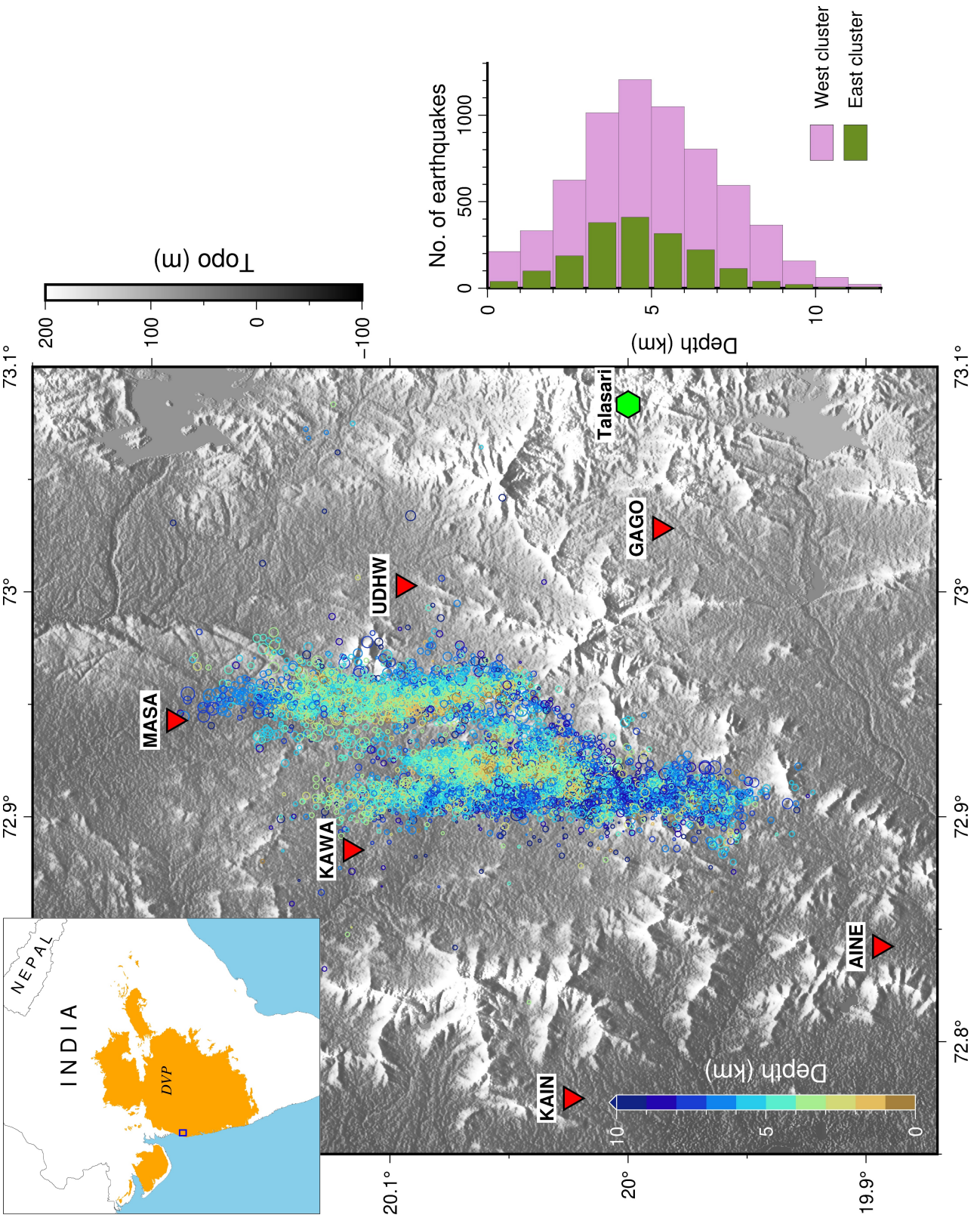
Topo (m)
200
100
0
−100
No. of earthquakes
0
500
1000
Depth (km)
0
5
10
West cluster
East cluster
73.1°
73°
72.9°
72.8°
20.1°
20°
19.9°
MASA
UDHW
KAWA
Talasari
GAGO
AINE
KAIN
Depth (km)
10
5
0
INDIA
NEPAL
DVP

Figure 1.

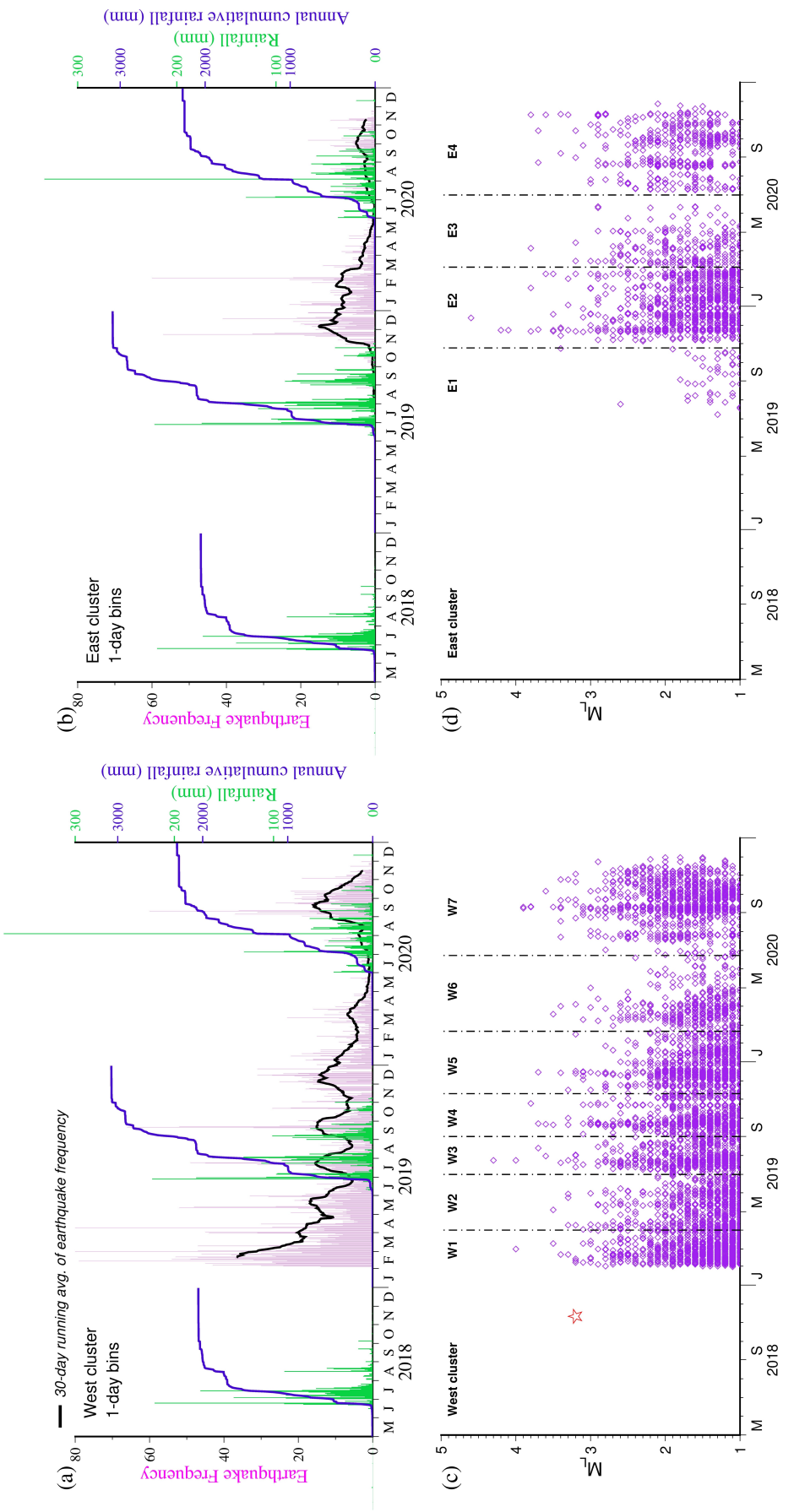
(a)
30-day running avg. of earthquake frequency
West cluster
1-day bins
Earthquake Frequency
Rainfall (mm)
Annual cumulative rainfall (mm)
(b)
East cluster
1-day bins
(c)
West cluster
W1
W2
W3
W4
W5
W6
W7
(d)
East cluster
E1
E2
E3
E4
M
J
S
2018
2019
2020

Figure 2.

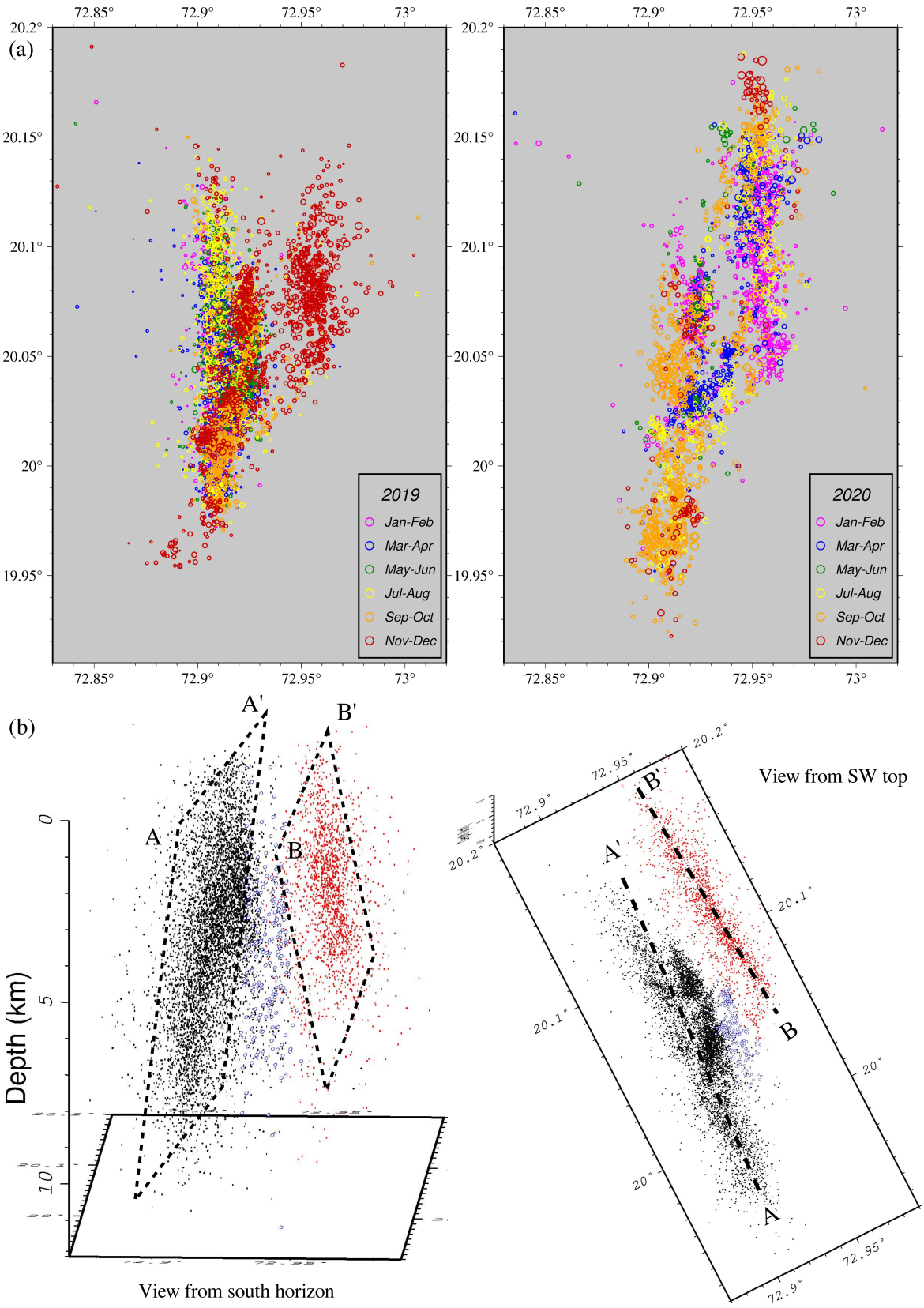
(a)
2019
Jan-Feb
Mar-Apr
May-Jun
Jul-Aug
Sep-Oct
Nov-Dec
2020
(b)
A
A'
B
B'
Depth (km)
View from south horizon
View from SW top

Figure 3.

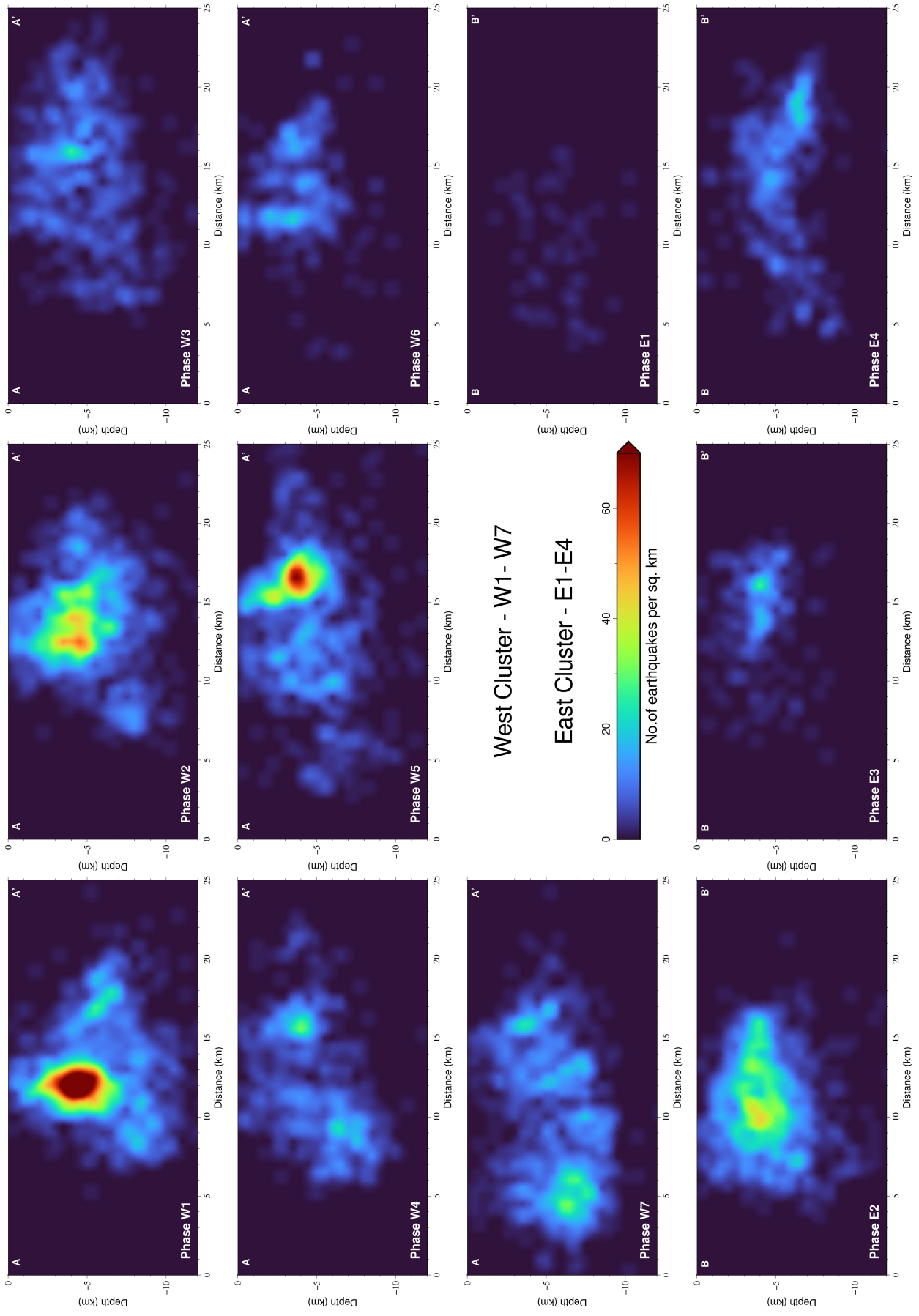
Phase W1
Phase W2
Phase W3
Phase W4
Phase W5
Phase W6
Phase W7
Phase E1
Phase E2
Phase E3
Phase E4
West Cluster - W1- W7
East Cluster - E1-E4
No.of earthquakes per sq. km
0
20
40
60
Depth (km)
Distance (km)
A
A'
B
B'

Figure 4.

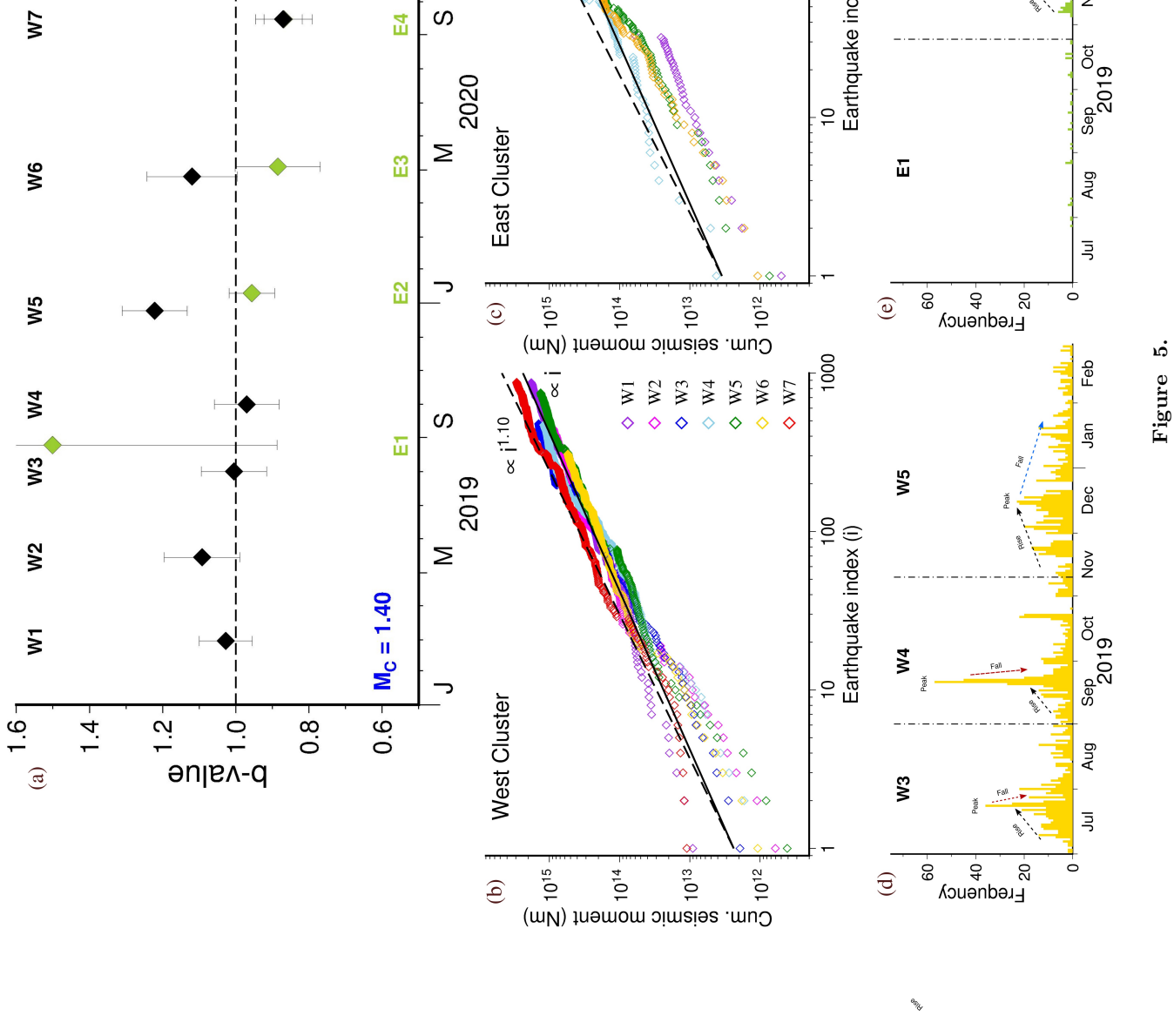
(a)
b-value
W1
W2
W3
W4
W5
W6
W7
M_C = 1.40
J
M
S
2019
E1
E2
E3
E4
(b)
West Cluster
Cum. seismic moment (Nm)
Earthquake index (i)
∝ $i^{1.10}$
∝ i
(c)
East Cluster
∝ $i^{1.15}$
(d)
(e)
Frequency
Peak
Fall
Rise
Jul
Aug
Sep
Oct
Nov
Dec
Jan
Feb

Figure 5.

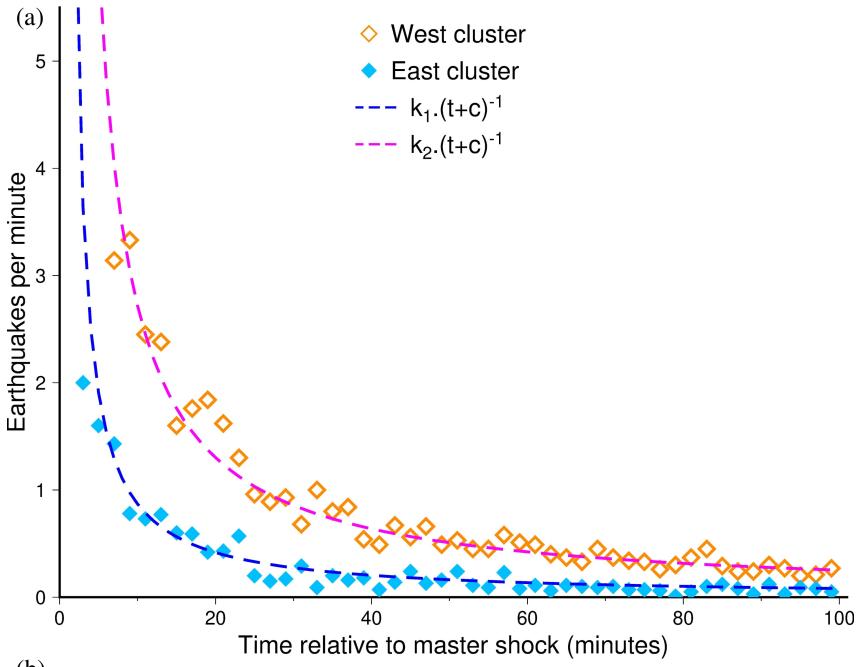
(a)
West cluster
East cluster
k1.(t+c)-1
k2.(t+c)-1
Earthquakes per minute
Time relative to master shock (minutes)

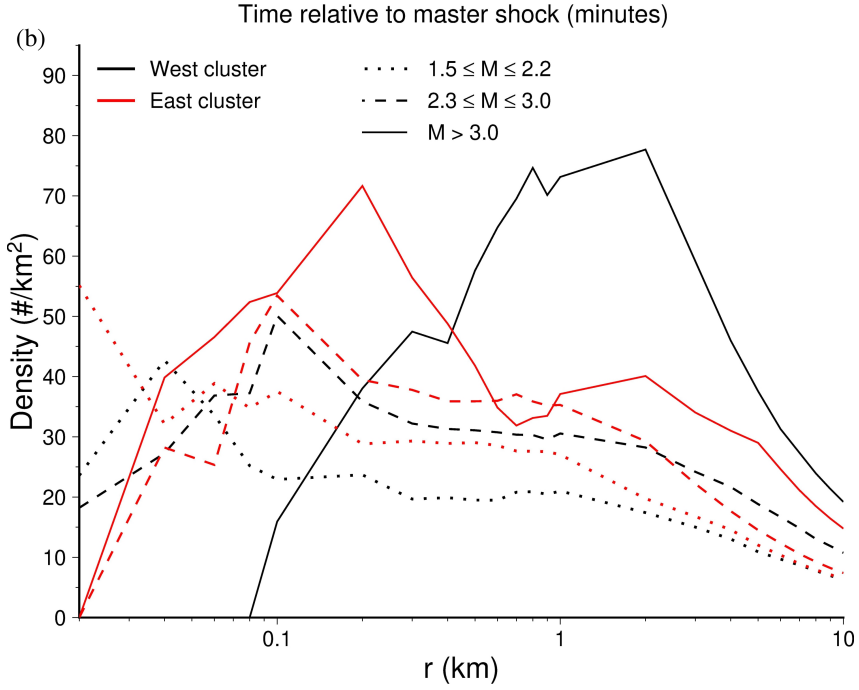
(b)
West cluster
East cluster
1.5 ≤ M ≤ 2.2
2.3 ≤ M ≤ 3.0
M > 3.0
Density (#/km2)
r (km)

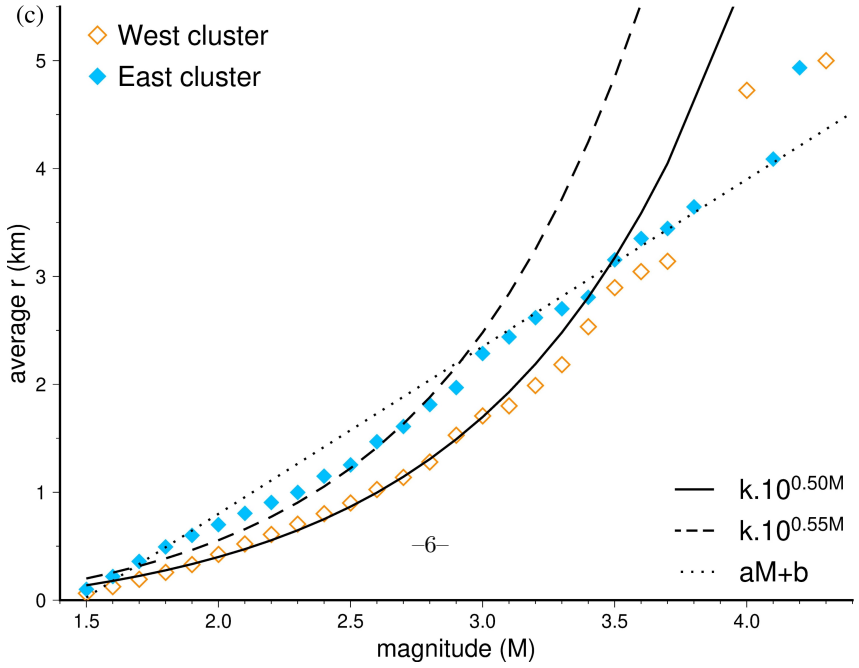
(c)
West cluster
East cluster
k.10^0.50M
k.10^0.55M
aM+b
average r (km)
magnitude (M)

Figure 6.

Supporting Information for "Stress triggering in a rain-induced earthquake swarm in the Palghar region, Western India"

Himangshu Paul[1,2]& M. Shekar[1]

[1]CSIR-National Geophysical Research Institute, Hyderabad, India.

[2]AcSIR-Academy of Scientific and Innovative Research, Ghaziabad, India

Contents

Corresponding author: Himangshu Paul, heman2007s@gmail.com

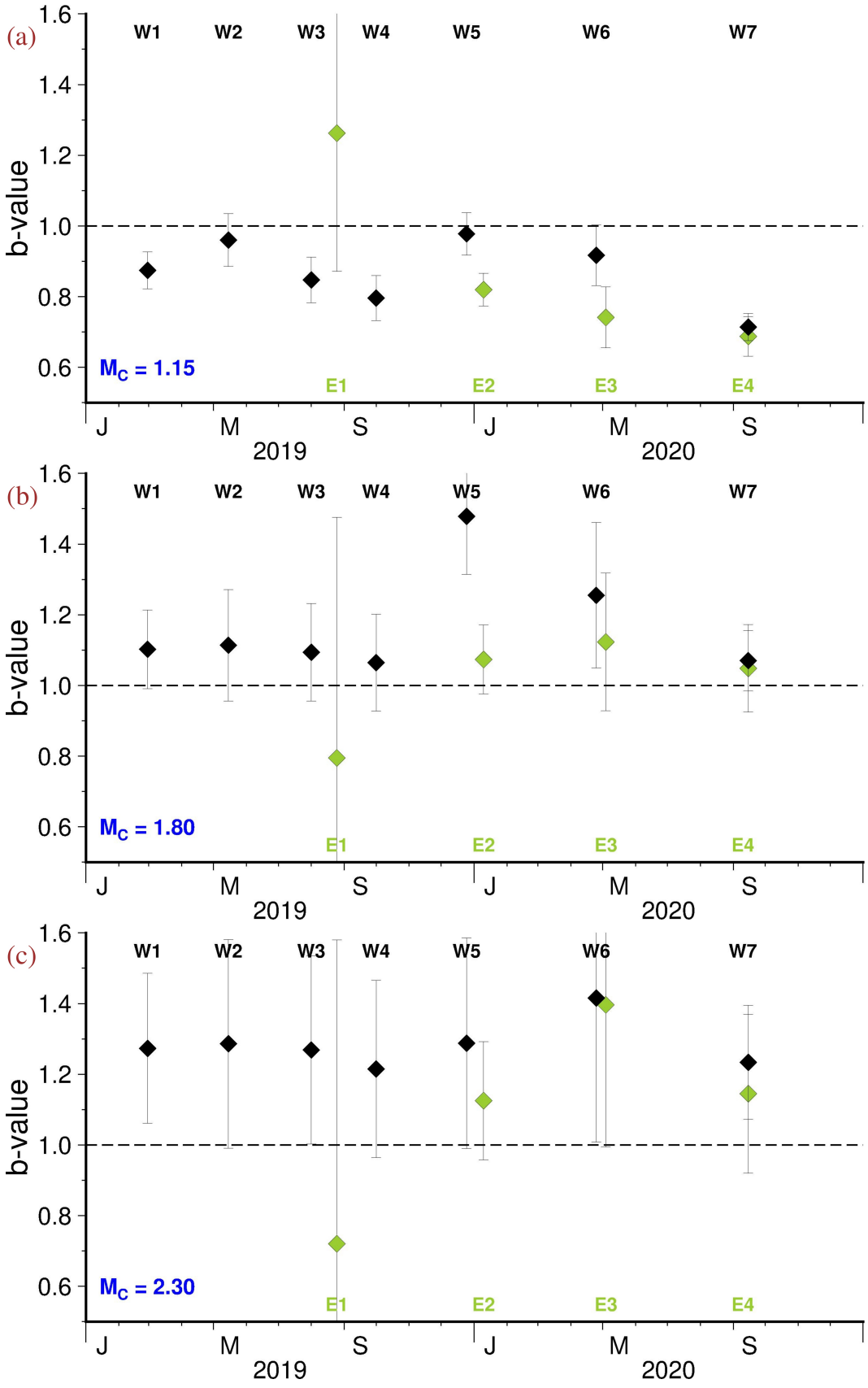

Figure S1. Temporal variation of b-values assuming (a) magnitude of completeness (M_C) = 1.15, (b) M_C = 1.8, and (c) M_C = 2.3. Maximum likelihood b-values and their standard errors are indicated for different phases of the swarm in the west (black symbols) and east (green) clusters.

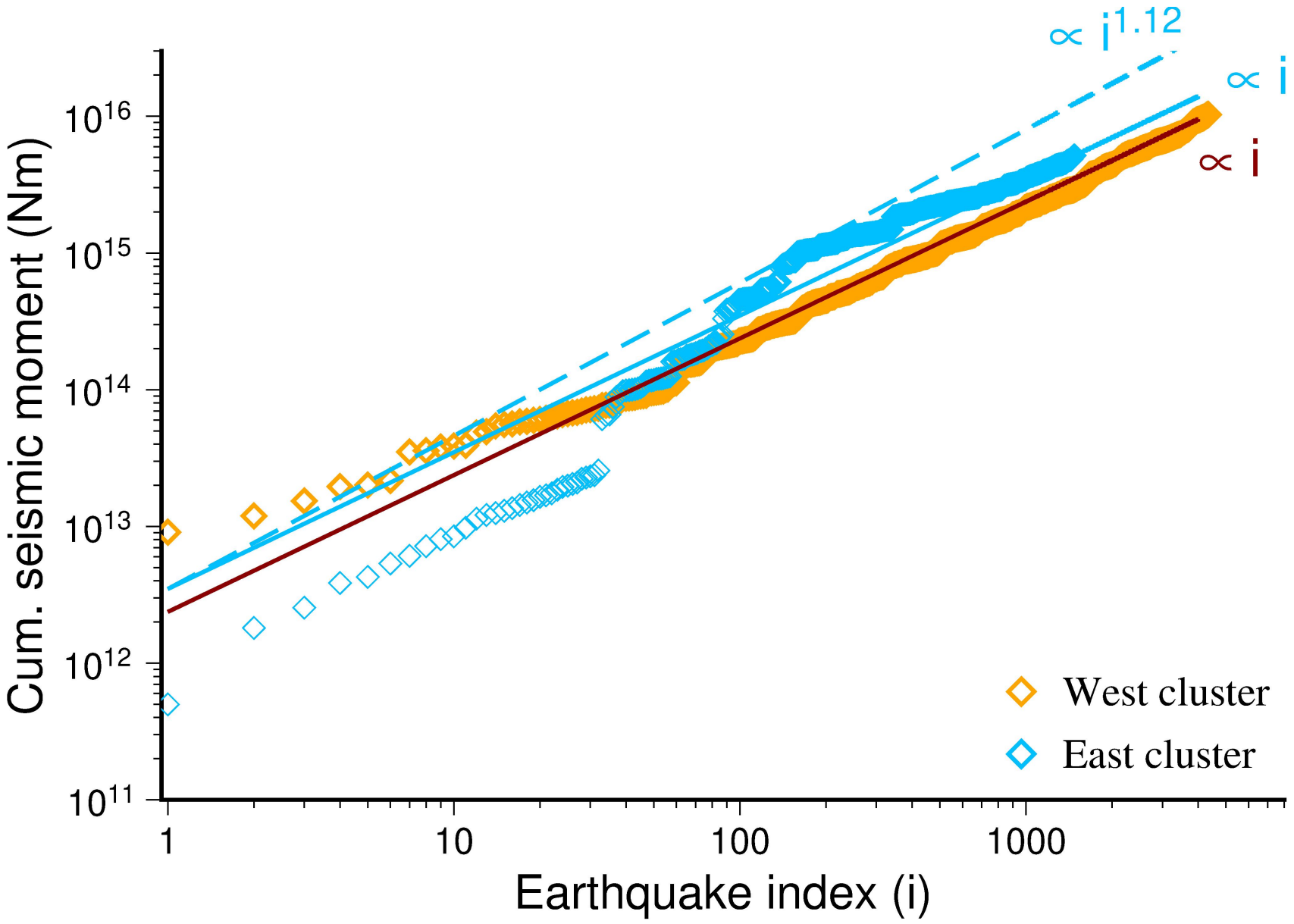

Figure S2. Cumulative seismic moment M_0 plotted as a function of earthquake index (i) for events in the west (orange) and east (sky-blue) clusters. Theoretical trend proportional to i is shown by a brown line for the west cluster. Corresponding trend lines for the east cluster, proportional to i and $i^1.12$ are shown in sky-blue.

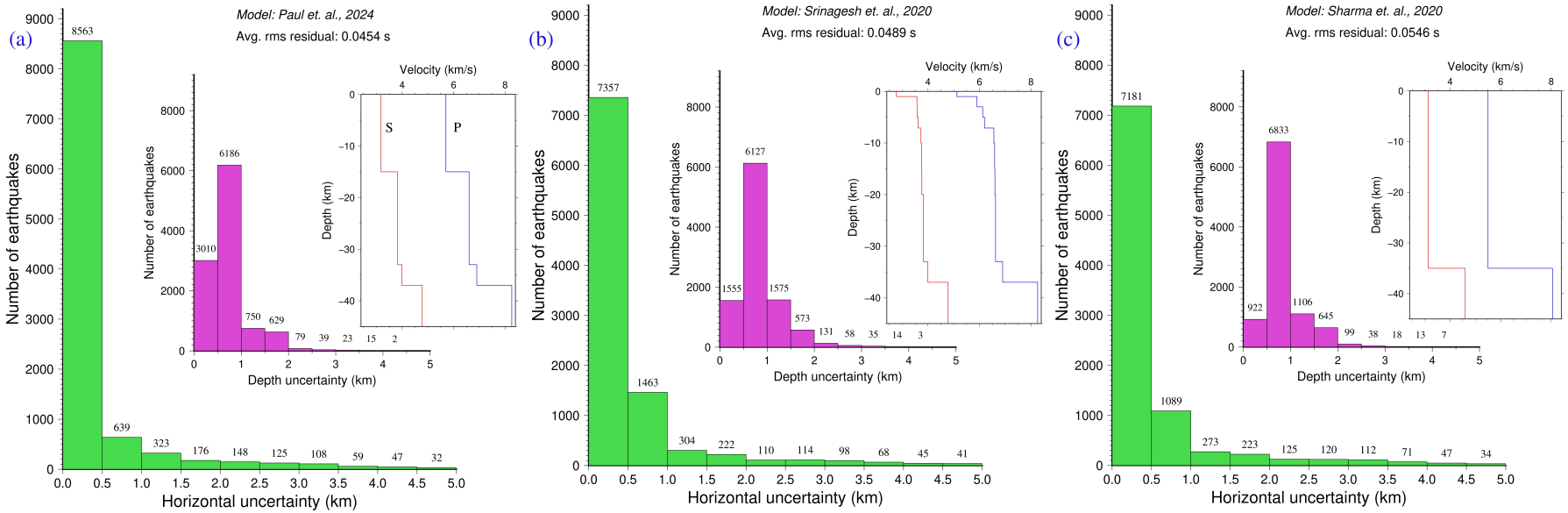

Figure S3. Histograms showing the number of earthquakes corresponding to different horizontal (green) and depth uncertainty (purple) bounds for three velocity models: (a) *Paul et al.*, []2024], (b) *Srinagesh et al.*, 2020, and (c) *Sharma et al.*, 2020. P- and S-velocity variations are shown to the right of each panel. The final RMS residual for each model is indicated at the top.

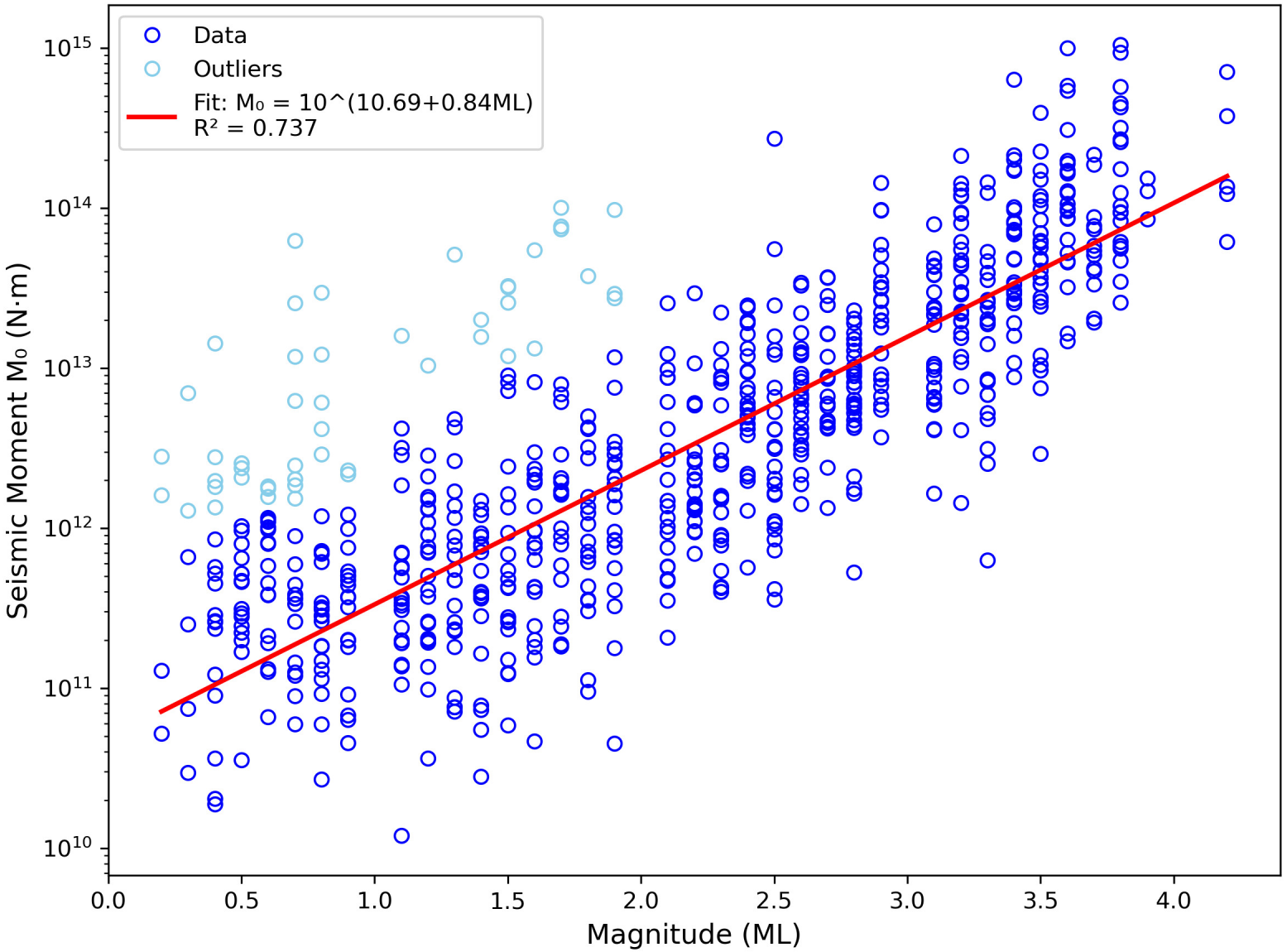

Figure S4. Calibration of the local magnitude (M_L) vs seismic moment (M_0) relationship. M_0 obtained by spectral fitting across all stations for a set of ∼190 events are plotted as a function of catalogue M_L values (blue circles). Anomalously high M_0 values at low M_L (<2) are considered outliers (light blue). The M_L-M_0 relationship is obtained from tbe best-fitting regression line (red).

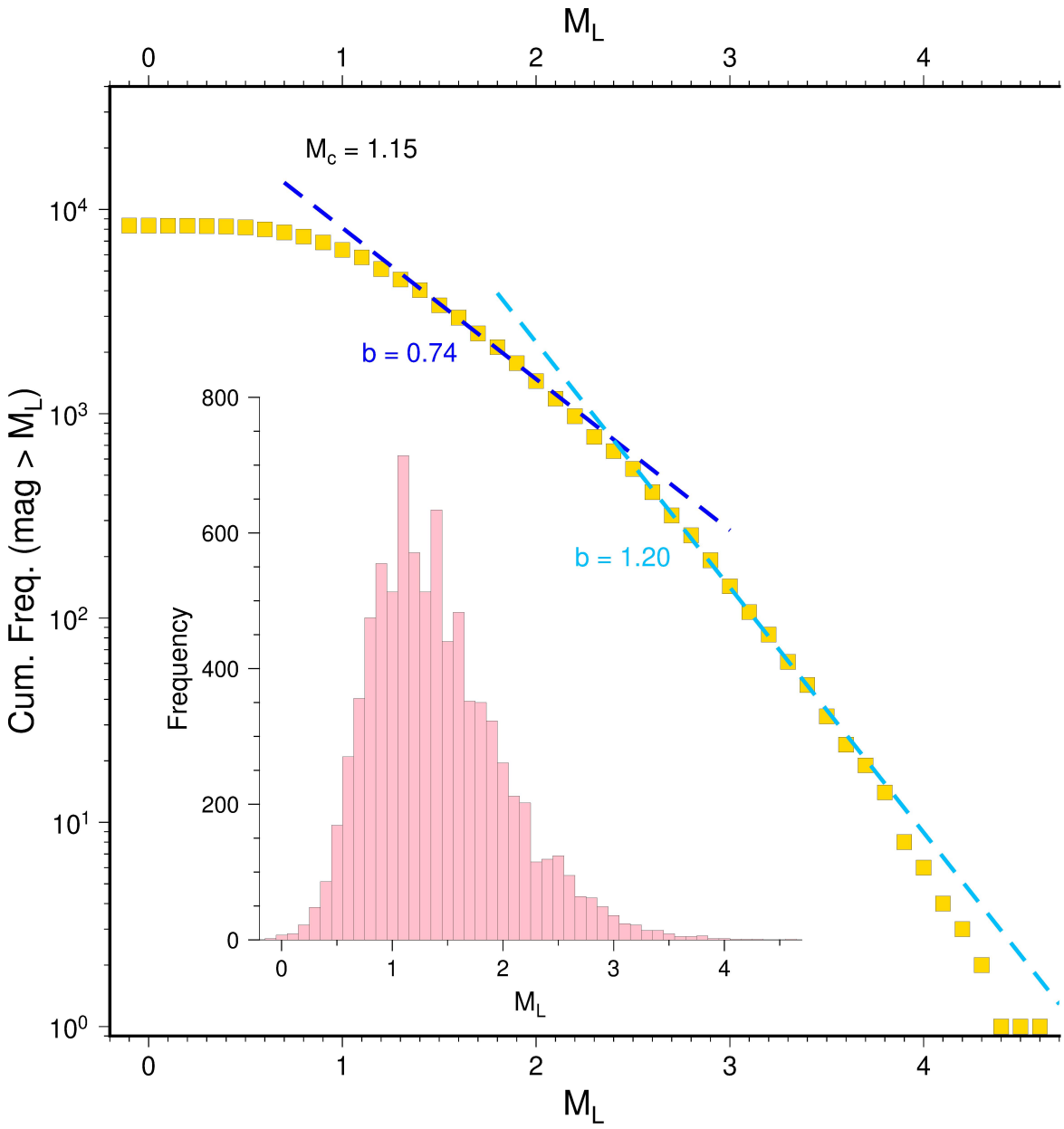

Figure S5. Frequency-magnitude distribution for all the well-located earthquakes between January 2019 and November 2020 is shown. The magnitude of completeness (M_C) is estimated to be 1.15 using the maximum curvature method. The b-values, derived from best-fitting slopes (shown in different colour) vary across different sections of the frequency-magnitude distribution. The magnitude histogram of the earthquakes is shown in the inset.